Nuclear Science and Techniques (2026) 37:43
https://doi.org/10.1007/s41365-025-01866-2

Real-time reconstruction and discrimination of pile-up neutron and gamma signals via bipolar cusp-like pulse shaping in NaIL scintillators

Jia-Xin Li[1,2] · Hui-Liang Hou[1,2] · Yue-Feng Huang[1,2] · Zhi-Min Dai[1,2]

Received: 8 June 2024 / Revised: 2 October 2024 / Accepted: 13 October 2024 / Published online: 9 January 2026

Abstract
At high count rates, pile-up events involving neutron and gamma signals result in inaccurate neutron counting and distortions in the energy spectrum. Additionally, a bipolar cusp-like pulse shaping algorithm based on an unfolding synthesis technique was proposed. This algorithm exhibits a narrow pulse shape, and the parallel design of the dual algorithms enables the recovery of pile-up signal amplitudes while preserving the distinct characteristics of neutron and gamma signals. The simplicity of the algorithm facilitates real-time neutron/gamma discrimination on an FPGA, allowing the energy spectra to be updated with each incoming signal. Furthermore, the algorithm can be readily tailored to various experimental conditions by adjusting the decay time constants. Multi-objective optimization reduces the need for manual parameter tuning by rapidly identifying the optimal parameters. Testing with a ^{241}Am-Be neutron source and a NaIL scintillator yielded a figure of merit (FoM) value of 2.11 and produced a clear energy spectrum even at high count rates.

Keywords FPGA · Pile-up · Neutron/gamma discrimination · NaIL · Multi-objective optimization

1 Introduction

High count rates commonly occur in radiation detectors, particularly in nuclear spectroscopy and nuclear reaction studies [1–3]. In these scenarios, the pile-up effect becomes a significant concern that undermines counting efficiency, as instruments may fail to accurately register each individual event when signals overlap [4]. Pile-up signals blur the distinctions between the energy levels of individual radiation events, hindering precise energy determination and distorting energy spectra [5, 6]. Furthermore, in neutron/gamma discrimination at high count rates, the pile-up effect complicates the accurate differentiation between neutron and gamma signals [7, 8]. This interference distorts the pulse shape, potentially leading to data misinterpretation and reduced detection performance [9]. Hence, addressing the pile-up effect is essential for improving the reliability and effectiveness of neutron/gamma discrimination techniques in high-count-rate conditions.

Scintillation detectors incorporating nuclei such as ^{6}Li, ^{10}B, and ^{157}Gd provide effective thermal neutron detection [10]; examples include Cs_2 $LiYCl_6$:Ce (CLYC) and Cs_2 $LiLaBr_6$:Ce (CLLB) [11–14]. Moreover, NaI scintillators co-doped with ^{6}Li (NaIL) offer excellent neutron/gamma discrimination due to the distinct pulse shapes produced by the high-energy reaction of ^{6}Li with thermal neutrons, thereby enhancing the detection and differentiation of gamma signals [15, 16]. Various pulse shape discrimination (PSD) methods have been proposed for these scintillator detectors, including the charge comparison method [12] and the zero-crossing method [17].

Machine learning techniques are increasingly employed for pulse shape discrimination [18]. For example, convolutional neural network (CNN) models trained on simulated

This work was supported by the National Natural Science Foundation of China (NSFC) (No. 12075308).

✉ Hui-Liang Hou
houhuiliang@sinap.ac.cn

✉ Zhi-Min Dai
daizhimin@sinap.ac.cn

[1] Shanghai Institute of Applied Physics, Chinese Academy of Sciences, Shanghai 201800, China

[2] University of Chinese Academy of Sciences, Beijing 100049, China

and experimental data have demonstrated effective discrimination of pile-up neutron/gamma signals [12, 19]. Liu et al. introduced a pulse-coupled neural network that achieved a 26.49% improvement in the figure of merit (FoM) compared with traditional charge comparison methods [20]. Although research [21] has explored the use of neural networks for neutron/gamma discrimination and online data processing, obtaining sufficient labeled data for effective training remains a challenge. Developing an accurate machine learning model for neutron/gamma discrimination requires a substantial reference dataset encompassing both neutron and gamma events [22]. Furthermore, neutron sources also emit gamma rays, complicating the separation of the two radiation types. Extracting datasets from mixed radiation fields and accurately labeling the signals are laborious tasks. Additionally, changes in measurement conditions, such as differences in detectors, radiation sources, or distances, may necessitate the reacquisition of reference datasets for model retraining. Labeled datasets often include misclassified samples due to overlapping gamma and neutron arrival time distributions and the presence of natural background radiation [23].

Machine learning techniques can identify patterns in large datasets that capture subtle differences between neutron and gamma signals, whereas digital signal processing (DSP) can further enhance these differences by transforming the signals without requiring extensive model training [24]. Rather than simply rejecting pile-up signals and tolerating losses, DSP techniques analyze the complete information contained in overlapping pulses, thereby retrieving signal amplitudes and identifying signal types [25, 26].

Although a fast Fourier transform (FFT) can yield more distinctive signal features [14, 27], its inherent latency hampers real-time discrimination under high flux. Similarly, while the wavelet transform (WT) has been employed to extract signal features [28, 29], selecting the optimal wavelet basis typically requires an iterative testing process. Optimization techniques such as the antilion algorithm and particle swarm optimization have also been applied to resolve second-order pile-up issues at high counting rates [30, 31]; these methods achieve high amplitude recovery accuracy but require long processing times.

Pulse shaping, on the other hand, enhances the distinct temporal features of neutron and gamma signals. Any pulse shape can be approximated using methods such as the z-transform derivation [20] or the unfolding synthesis technique [32, 33], both of which are computationally efficient and suitable for real-time implementation on FPGAs. Moreover, pulse shaping methods not only facilitate waveform discrimination but also improve the signal-to-noise ratio and energy resolution in spectroscopy [34, 35]. Although slow shapers yield high energy resolution in spectral analysis, they perform less effectively than fast shapers at high count rates. For example, Nakhostin reduced the probability of pulse pile-up by shortening the pulse width [36], and Wen et al. demonstrated that a neutron/gamma signal maintained a distinct zero-crossing time when processed through a fast triangular shaper [17]. Additionally, a combination of a trapezoidal shaper and a sawtooth shaper has been used to achieve PSD while compensating for the ballistic deficit [37]. The cusp-like shape, which exhibits a narrower width than the triangular shape for identical rise and fall times, facilitates pile-up rejection [2]. However, unipolar shaping can lead to baseline shift [20]; in principle, these shifts can be mitigated by employing bipolar pulse shapes. Indeed, the bipolar trapezoidal and bipolar cusp-like shapers presented in [38, 39] demonstrated that bipolar pulse shaping can achieve baseline restoration at high count rates. Despite the widespread use of pulse shaping techniques in online nuclear instrumentation measurements, challenges remain in achieving effective neutron–gamma discrimination at elevated count rates while preserving accurate amplitude recovery.

The aim of this study is to propose a bipolar cusp-like pulse shaping algorithm designed to correct pile-up signals under high radiation flux. Based on the unfolding synthesis technique, the algorithm exploits a distinctive narrow pulse width to facilitate the reconstruction of pile-up signals originating from NaIL scintillators. A notable advantage of the proposed algorithm is its suitability for real-time implementation on FPGA platforms. In addition, multi-objective optimization is employed to minimize manual parameter tuning by determining the optimal decay time constants. Testing in a mixed radiation field generated by a ^{241}Am-Be neutron source confirmed the algorithm's capability for pile-up correction and energy spectrum recovery.

2 Method

2.1 Bipolar cusp-like pulse shaping algorithm

The interaction between the scintillator material and incident particles results in the emission of light, which is subsequently collected by a photomultiplier tube (PMT) to produce an electrical signal. This signal is generally characterized by a bi-exponential model. Following digitization by a high-speed ADC with sampling period ΔT, the bi-exponential model in the discrete-time domain can be expressed as

$$x(n) = A_1 \cdot e^{-n\cdot\Delta T/\tau_1} - A_2 \cdot e^{-n\cdot\Delta T/\tau_2}, n \geq 0, \quad (1)$$

where τ_1 and τ_2 represent the decay time constants for the slow and fast components, respectively, and are determined by factors such as the properties of the scintillator material and the design of the PMT and preamplifier. Here, A_1 and A_2 denote the pulse amplitudes, which also govern the signal

width. The subsequent derivation is based on this standard bi-exponential model.

The unfolding synthesis technique enables the construction of virtually any pulse shape, either exactly or as a close approximation [32]. It finds applications in linear signal processing systems, whether they are time-invariant or time-varying. The bipolar cusp-like pulse shaping algorithm consists of two main components: an unfolding system and a synthesis system.

The purpose of the unfolding system is to deconvolute the nuclear signal into unit impulses. The unfolding equation for a single-exponential signal is provided in [32]. In the discrete-time domain, a single-exponential signal is defined as

$$h(n) = \begin{cases} a^n, n \geq 0, \\ 0, n < 0, \end{cases} \tag{2}$$

$$a = e^{-\Delta T/\tau}, \tag{3}$$

where a is the exponential base [32], a constant gain determined by the ADC sampling rate and the decay time constant of the single-exponential signal. Equation 2 can be rewritten in the following recursive form:

$$h(n) = a \cdot h(n-1), n > 0, h(0) = 1. \tag{4}$$

Equation 4 shows that the single-exponential signal defined in Eq. 2 can be unfolded via appropriate scaling and shifting. The operational algorithm for unfolding a single-exponential signal is described by the following equation [32]:

$$z(n) = h(n) - a \cdot h(n-1). \tag{5}$$

For $n > 0$, Eq. 5 becomes

$$z(n) = h(n) - a \cdot h(n-1) = a^n - a \cdot a^{n-1} = a^n - a^n = 0. \tag{6}$$

For $n = 0$, Eq. 5 becomes

$$z(0) = h(0) - a \cdot h(-1) = a^0 - 0 = 1. \tag{7}$$

Based on the definition of a single-exponential signal in Eq. 2, all sampling points before $n = 0$ are zero. Thus, $z(n)$ is defined as

$$z(n) = \begin{cases} 1, n = 0, \\ 0, \text{elsewhere}, \end{cases} \tag{8}$$

which is the same as the definition of $\delta(n)$. Therefore, the unfolding equation for a single-exponential signal is defined as

$$\delta(n) = h(n) - a \cdot h(n-1). \tag{9}$$

However, the actual nuclear signal is better approximated by a bi-exponential model than by a single-exponential model. To address this, [40] demonstrated that using two sequential unfolding equations can significantly reduce the width of a nuclear signal, allowing it to approximate a unit impulse signal. As shown in Fig. 1, Eq. 9 is applied twice in the unfolding system. In this process, a_1 and a_2 are determined using τ_1 and τ_2 from Eq. 1, respectively. Implementation of the unfolding system thus requires only the determination of the two decay time constants of the bi-exponential signal.

The function of the synthesis system is to reconstruct the unit impulse into a target pulse shape through addition, multiplication, and accumulation. This reconstruction requires

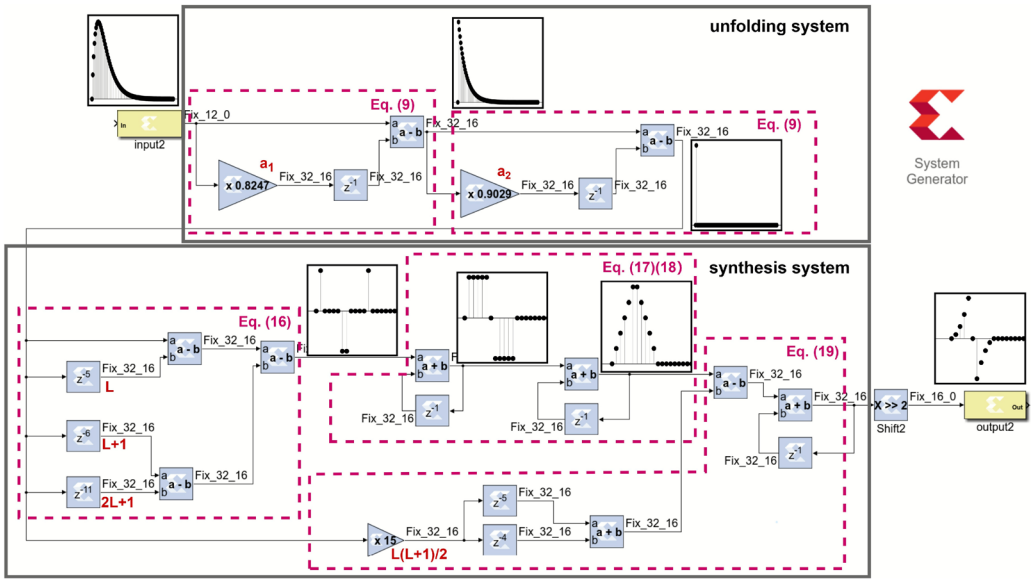

Fig. 1 Block diagram of the bipolar cusp-like shaping algorithm constructed in MATLAB Simulink

determining the target pulse shape, followed by differentiating it to obtain a linear combination of weighted and shifted unit impulses. Based on this linear combination, the synthesis equations for the target pulse shape are derived through accumulation. A bipolar cusp-like shape was selected for this study because of its narrow width, which is well suited for high-count-rate measurements, and its bipolar nature, which helps prevent baseline drift. The target bipolar cusp-like signal can be expressed as

$$y(n) = \begin{cases} 0, & n < 0, \\ (n+1)\cdot(n+2)/2, & 0 \le n < L-1, \\ 0, & n = L-1, \\ -(2L-1-n)\cdot(2L-n)/2, & L \le n < 2L, \\ 0, & n \ge 2L, \end{cases} \tag{10}$$

where L determines the duration of the rising and falling edges. Equation 10 is a piecewise function comprising two quadratic curves, as shown in Fig. 2f. Applying a discrete difference to Eq. 10 results in

$$y'_{\text{true}}(n) = \begin{cases} 0, & n < 0, \\ n+1, & 0 \le n < L-1, \\ -L(L+1)/2, & n = L-1, \\ 2L-n, & L \le n < 2L. \\ 0, & n \ge 2L. \end{cases} \tag{11}$$

To remove the discontinuity at $n = L-1$, the differentiated result is adjusted as

$$y'(n) = y'_{\text{true}}(n) + \frac{L(L+1)}{2}\cdot[\delta(n-L) - \delta(n-L+1)], \tag{12}$$

and the piecewise function representation becomes

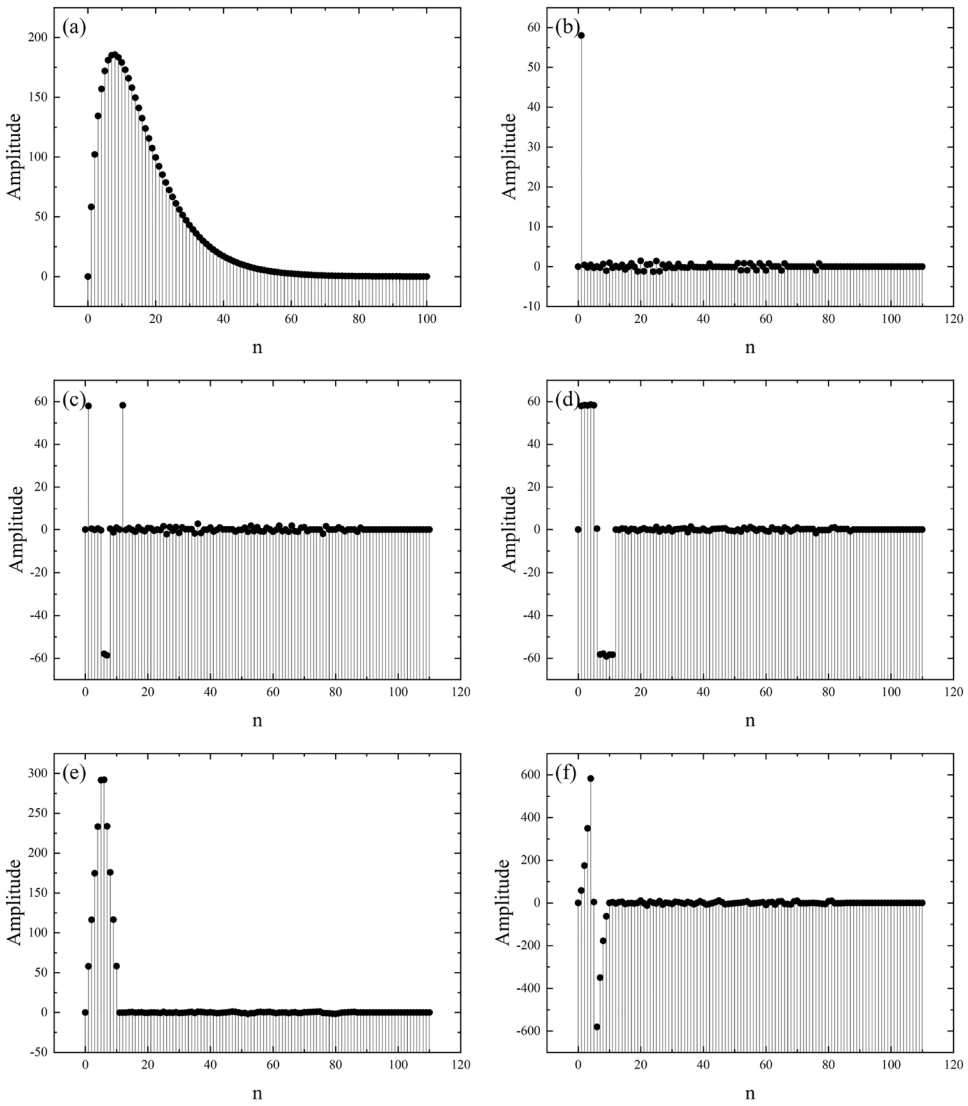

Fig. 2 **a** Input bi-exponential signal and **b** its unfolding result. **f** Target bipolar cusp-like signal and its derivatives: **e** first, **d** second, and **c** third derivatives

$$y'(n) = \begin{cases} 0, & n < 0, \\ n+1, & 0 \le n < L, \\ 2L-n, & L \le n < 2L, \\ 0, & n \ge 2L, \end{cases} \tag{13}$$

which is considered the first-order difference of Eq. 10 in this paper. As shown in Fig. 2e, $y'(n)$ exhibits the shape of an isosceles trapezoid. Differentiating Eq. 13 yields

$$y''(n) = \begin{cases} 0, & n < 0, \\ 1, & 0 \le n < L, \\ 0, & n = L, \\ -1, & L+1 \le n < 2L+1, \\ 0, & n \ge 2L+1. \end{cases} \tag{14}$$

The unit step function $u(n)$ is used to represent the interval of the piecewise function in Eq. 14 in a discrete form, which can be expressed as

$$y''(n) = u(n) - u(n-L) - [u(n-(L+1)) - u(n-(2L+1))], \tag{15}$$

whereas the third-order difference is expressed as

$$y'''(n) = \delta(n) - \delta(n-L) - [\delta(n-L-1) - \delta(n-2L-1)], \tag{16}$$

which is a linear combination of weighted and shifted unit impulses. The equations for the synthesis system can be derived by using the $\delta(n)$ signal obtained from the unfolding system to construct Eq. 16, followed by three accumulation operations:

$$y''(n) = y''(n-1) + y'''(n), \tag{17}$$

$$y'(n) = y'(n-1) + y''(n), \tag{18}$$

$$y(n) = y(n-1) + y'(n) - \frac{L(L+1)}{2} \cdot [\delta(n-L) - \delta(n-L+1)]. \tag{19}$$

Xilinx System Generator (XSG) is a powerful tool for developing digital signal processing (DSP) systems using Xilinx FPGAs. It is an essential component of the Xilinx design suite and offers a high-level graphical environment for algorithm development and hardware implementation. The block diagram of the bipolar cusp-like shaping algorithm, defined by Eqs. 9, 16, 17, 18, and 19, is illustrated in Fig. 1. The proposed algorithm comprises only a few adders and multipliers, rendering its structure simple and conducive to real-time FPGA implementation. The output bit-width limits (labeled in Fig. 1) for each block indicate that the algorithm operates in fixed-point arithmetic. Consequently, each time the signal passes through a block, quantization noise is introduced due to rounding. Under high-count-rate conditions, L was fixed at five in this study, resulting in a short rising and falling edge, as shown in Fig. 2f. For different types of signals from various detectors, only a_1 and a_2 need to be adjusted.

Setting A_1 and A_2 to 1000, $\Delta T/\tau_2$ to 1/10, and $\Delta T/\tau_2$ to 1/6 in Eq. 2 artificially produces a double exponential signal as:

$$x(n) = 1000 \cdot (e^{-n/10} - e^{-n/6}), n \ge 0. \tag{20}$$

The parameters of the unfolding system, shown in Fig. 1, correspond to the decay time constants in Eq. 20. Processing Eq. 20 with the algorithm illustrated in Fig. 1 produced the results shown in Fig. 2, which display the unfolding and synthesis process for a bi-exponential signal. As shown in Fig. 2b, the standard bi-exponential signal is deconvoluted into a unit impulse through the unfolding system containing two decay time constants. A noticeable deviation from the ideal shape appears during the shaping process, as the amplitude fluctuates around 0 for $n > 1$, rather than reaching 0 precisely. This occurs because all mathematical operations in the algorithm are implemented using fixed-point arithmetic to achieve fast computation speeds. The parameter a, which acts as a gain constant in the unfolding system, has restricted precision due to its fixed-point representation. Consequently, despite the real-time DSP advantages offered by FPGAs, non-floating-point operations may incur some precision loss, leading to computational results that deviate from those obtained via computer calculations. Using higher-end FPGAs with greater resources and improved performance can allow for an increased bit width in each operation, thereby rendering the precision loss more tolerable.

2.2 Particle classification criteria and amplitude recovery

The neutron signal is narrower than the gamma signal in the output of the NaIL detector used in this study. Figure 3a illustrates the neutron and gamma signals with distinct pulse widths, along with artificially constructed pile-up events formed by combining these two signals. In these experiments, one signal was delayed by eight clock cycles and added to the other to create a pile-up event. Because neutron and gamma signals have different decay time constants, a pulse shaping algorithm optimized for one decay constant produces distinct shaping results for each signal type.

The blue curve in Fig. 3c shows the shaping result of the red curve in Fig. 3a when processed using the pulse shaping algorithm for gamma (PSAG). PSAG is designed to match the decay time constants of the gamma signal, rendering the gamma signal closer to a bipolar cusp-like shape after shaping. However, the neutron signal, which decays faster than the gamma signal, does not conform to PSAG's parameters and exhibits an overshoot when returning to the baseline. In

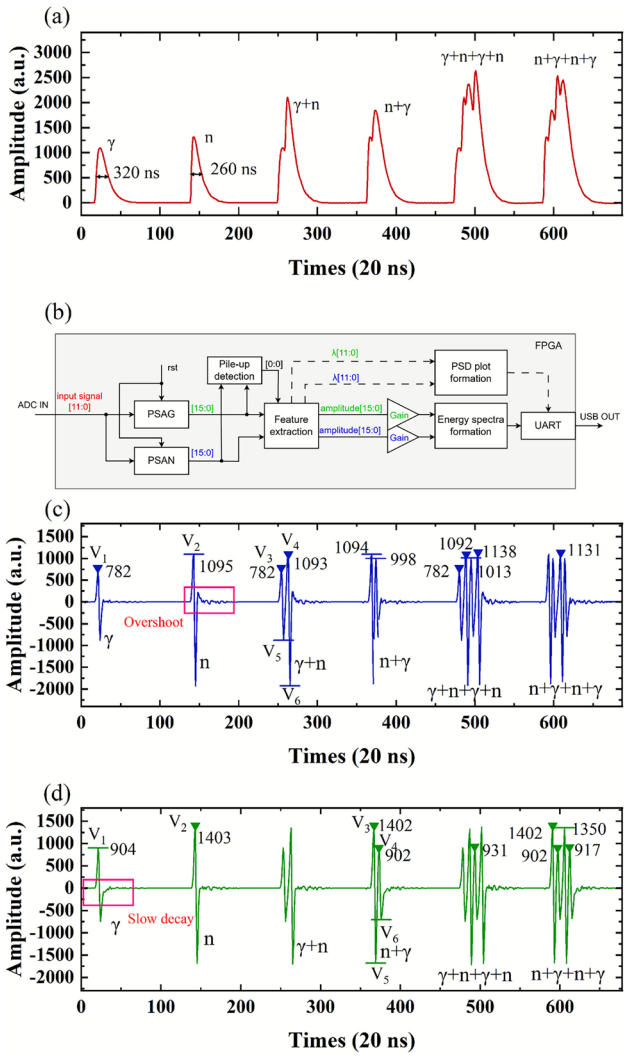

Fig. 3 (Color online) **a** Input neutron, gamma, and pile-up signals. **b** Signal processing flow on the FPGA. **c** Shaping result obtained by the PSAG. **d** Shaping result obtained by the PSAN

n+γ or n+n pile-up cases, the later pulse is superimposed on this overshoot, leading to inaccurate amplitude recovery.

Conversely, the green curve in Fig. 3d displays the shaping result of the red curve in Fig. 3a when processed with the pulse shaping algorithm for neutron (PSAN). Unlike PSAG, PSAN shapes the neutron signal into a bipolar cusp-like form; however, when PSAN is applied to the gamma signal, the slower decay prevents it from returning to the baseline within five clock cycles. In γ+n and γ+γ pile-up events, the amplitude of the latter signal is lower than its true value because the previous gamma signal does not return to the baseline quickly. Thus, PSAG produces an overshoot for neutron signals while PSAN yields a slow decay for gamma signals. Both overshoot and slow decay distort the preceding pulse, preventing the subsequent pulse's amplitude from recovering to its original value.

Nevertheless, the γ+n event shown in Fig. 3c and the n+γ event in Fig. 3d exhibit satisfactory amplitude recovery. In Eq. 21, the variable ε quantifies the amplitude recovery of the pile-up signal, with smaller values indicating better recovery. The amplitude of the preceding signal is typically unaffected ($V_1 = V_3$), and the later signal in a pile-up event can only be approximately restored if the preceding signal returns to the baseline without overshoot or slow decay ($V_2 \approx V_4$). In the PSAG results, the single shaped neutron signal has an amplitude of 1095. Because PSAG matches the gamma decay constants, the gamma signal returns to the baseline without overshoot in the γ+n event, and the recovered neutron amplitude is approximately 1093, yielding an ε value of 2. Similarly, in the PSAN results the single shaped gamma signal has an amplitude of 904, and in the n+γ event, the recovered gamma amplitude is about 902, also yielding an ε value of 2.

$$\varepsilon = |V_2 - V_4|. \tag{21}$$

In both PSAG and PSAN, the troughs of the shaped neutron signals are markedly larger than their peaks due to the faster decay of neutron signals. The ratio of the peak to the sum of the peak and trough serves as the criterion for particle-type discrimination, as defined in Eqs. 22 and 23. The values of λ_1 and λ_2 were computed using the Xilinx Vivado Divider IP core operating in Radix-2 mode, which divides two 12-bit unsigned numbers to yield a 24-bit result that includes a 12-digit fractional part. This process results in a latency of 26 clock cycles. Because both λ_1 and λ_2 must be less than 1, the 12-digit fractional part is used as the horizontal coordinate of the PSD plot. The PSD measurements allowed us to obtain the λ values ($\lambda_{\text{standard}}$) used by PSAN and PSAG to distinguish between neutron and gamma signals. In Eq. 24, the variable σ represents the discrimination power between neutron and gamma signals, with higher values being preferable.

$$\lambda_1 = |V_3|/(|V_3| + |V_5|), \tag{22}$$

$$\lambda_2 = |V_4|/(|V_4| + |V_6|), \tag{23}$$

$$\sigma = |\lambda_1 - \lambda_2|. \tag{24}$$

Both ε and σ are used as evaluation metrics in the multi-parameter optimization, and only the λ value is computed on the FPGA for classifying neutron/gamma signals.

In summary, although both PSAG and PSAN can discriminate between the two signals, accurate amplitude recovery requires dual-channel shaping utilizing both PSAG and PSAN. Thanks to the FPGA's parallel-processing capability, dual-channel shaping does not introduce delays. Figure 3b shows the signal processing flow on the FPGA, where the 12-bit signal from the ADC is processed in parallel through

PSAG and PSAN to produce two 16-bit outputs. The number of pile-up events in the signals processed by PSAG and PSAN is minimal, primarily due to the reduction in signal widths. A feature extraction module simultaneously extracts signal characteristics (signal type, peaks, and troughs) from the outputs of the PSAN and PSAG algorithms, while a pile-up detection module identifies pile-up events by calculating the interval between the current and previous signal peaks.

First, both algorithms produce a classification result for the same signal using $\lambda_{\text{standard}}$ determined from the PSD plots; the discrimination result is considered valid only if both algorithms yield the same classification outcome. Following classification, the valid amplitude output is selected. In Fig. 3c and d, the valid amplitude output is marked with a triangle symbol. For isolated signals (where the current signal peak is more than 50 sampling points away from the previous peak), the gamma signal amplitude from PSAG is valid, while the neutron signal amplitude from PSAN is valid. When the current signal peak is less than 50 sampling points away from the previous peak and the preceding signal is a neutron signal, the current amplitude from PSAN is considered valid. Conversely, if the previous signal is a gamma signal, the current amplitude from PSAG is taken as valid. Therefore, γ+n and γ+γ outputs from PSAG are valid, and n+γ and n+n outputs from PSAN are valid.

For the same neutron signal, PSAG yields an amplitude of 1095 while PSAN produces an amplitude of 1403, indicating that PSAN has a higher output amplitude. This selection approach enhances the overall neutron signal amplitudes, thereby mitigating misclassification between neutron and gamma signals in the low-energy region. In addition, due to the generally higher amplitudes of the PSAN outputs, the valid neutron amplitude from PSAG is multiplied by a gain factor of 1.282 for the neutron response spectrum, and the valid gamma amplitude from PSAN is multiplied by a gain factor of 0.865 for the gamma spectrum.

However, the dual-channel shaping algorithm fails to respond adequately to multiple consecutive short-interval pulses. In the γ+n+γ+n event shown in Fig. 3c, the first two pulses exhibit amplitude recovery similar to that observed in the n+γ event, but the two subsequent pulses cannot be accurately recovered due to the overshoot produced by the neutron signal. In this scenario, the algorithm erroneously considered the amplitude of the last neutron signal (1138) as valid, although it should have been 1095. Similarly, in the n+γ+n+γ event shown in Fig. 3d, because the preceding signal to the last gamma signal is a neutron signal, the last gamma signal amplitude of 917 is taken as valid, although the expected value is 904. Thus, even though dual-channel shaping rectifies the inaccurate amplitude recovery associated with two pile-up signals, the failure of the pulse to rapidly return to baseline in these events leads to poor amplitude recovery for any subsequent signals.

2.3 Multi-objective optimization for parameter determination

As with other pulse shaping algorithms, the decay time constants are the key parameters for this algorithm. Typically, a preliminary fitting process based on an analytical exponential model is conducted on a computer to obtain these parameters. However, discrepancies between the actual nuclear signal and the ideal bi-exponential model often render complete fitting impossible. Consequently, the fitting process and subsequent algorithm tests are frequently performed by trial and error, and the decay time constants derived from such fitting may not yield smooth pulse shaping (as illustrated in Fig. 2), thereby necessitating manual adjustments to achieve optimal discrimination.

To circumvent the need for manual adjustments, Gaussian mixture models and deep learning transformer models have been employed to identify pulse shape parameters [41, 42]. In this study, multi-objective optimization was employed to determine the optimal decay time constants, ensuring both effective neutron/γ discrimination (quantified by σ) and accurate amplitude recovery (quantified by ε).

The multi-objective optimization of the proposed algorithm was performed using the MATLAB function `gamultiobj` from the Global Optimization Toolbox. This function generates a set of optimal solutions along the Pareto front in the space of decision variables and employs a controlled elitist genetic algorithm—a variant of the Non-dominated Sorting Genetic Algorithm II (NSGA-II) [43]. In genetic algorithms, the controlled elitist approach is notable for its emphasis on preserving population diversity, even at the expense of selecting individuals with lower fitness. This strategy is pivotal for steering convergence toward an optimal Pareto front, where the solutions balance the conflicting objectives (σ and ε). Maintaining diversity within the population plays a crucial role as the algorithm unfolds.

Two key mechanisms, namely `ParetoFraction` and `DistanceMeasureFcn`, are instrumental in controlling elitism. ParetoFraction regulates the number of individuals designated as elite members on the Pareto front, ensuring a balanced representation of optimal solutions. Meanwhile, the `DistanceMeasureFcn` actively promotes diversity along the Pareto front by favoring individuals that are spatially separated, thereby mitigating the risk of premature convergence toward suboptimal solutions.

A key stopping criterion for the algorithm is the spread assessment—a metric that monitors the extent of movement along the Pareto front. If the spread diminishes to a predefined threshold, indicative of stagnation or limited exploration of the solution space, the algorithm terminates. This approach not only safeguards against premature convergence but also encourages a thorough exploration of the solution landscape, ultimately fostering the discovery of robust and

diverse Pareto-optimal solutions. After performing multi-objective optimization based on the amplitude recovery and discrimination performance for the four pile-up events (γ+γ, γ+n, and n+γ, n+n), the optimal decay time constants were selected from the Pareto front.

3 Experimental setup

Data acquisition and algorithm tests were performed using a 30 mCi ^{241}Am-Be neutron source. Varying the concentration of ^{6}Li yielded distinct characteristics in the neutron and gamma signals. For instance, NaI:Tl detectors containing 1% ^{6}Li can convert a conventional NaI:Tl detector into a neutron/gamma spectroscopic dual-mode detector without compromising neutron detection efficiency [44]. To achieve a higher count rate, a Φ50.8 mm × 50.8 mm ^{6}Li-enriched (95%) NaI:Tl scintillator with 1% ^{6}Li doping was placed adjacent to the source outlet. As shown in Fig. 4, the detector was placed inside a polyethylene enclosure, and a lead layer was wrapped around it to reduce excessive gamma radiation. A preliminary check of the detector's response to gamma rays was performed using a ^{137}Cs gamma source, which yielded an energy resolution of 7.01% for the 662 keV full-energy peak.

A preamplifier was integrated into the PMT immediately behind the NaIL scintillator. The PMT CR105 was purchased from Beijing Hamamatsu Photon Techniques Inc. The electrical signals generated by the PMT were amplified directly without passing through transmission cables, thereby reducing noise interference. Subsequently, a discriminator was devised to process the nuclear signals produced by the preamplifier. This discriminator primarily comprises an A/D converter (AD9236), a Xilinx Artix 7 series FPGA (XC7A200TFBG484-2), a USB communication circuit, and power supply circuits. The input signal from the preamplifier underwent direct digitization using the AD9236, which employs a multistage differential pipelined architecture to provide 12-bit resolution at speeds of up to 80 Msps. Choosing a digitizer with an appropriate sampling rate involves a trade-off between performance and economy; research [45] has shown that a FoM better than 2.0 can be achieved at a 125 MHz sampling rate above 300 keV. In this study, the ADC sampling rate was 50 MHz, which minimizes hardware requirements. In addition, an internal reference voltage of 1 V was used, exhibiting a voltage error of 0.42% at 20° C. To mitigate the impact of temperature drift, the adoption of an additional external reference is recommended. The digitized signal was conveyed in parallel with the FPGA in complementary format. Real-time digital signal processing and spectrum formation were achieved using a single FPGA. The recorded energy spectra were stored in the BRAM on the FPGA, and the spectrum data were periodically transmitted to a host computer via a USB interface. Meanwhile, the entire discriminator was powered by a 5 V supply provided through the USB interface.

The research workflow comprised three main phases. Initially, multiple neutron and gamma signals were extracted from the discriminator and processed using MATLAB Simulink. Pile-up events (γ+γ, γ+n, n+γ, and n+n) with varying amplitudes were manually constructed to validate the pulse shaping algorithm for neutron/γ discrimination and amplitude recovery. Subsequently, a multi-objective optimization based on these pile-up signals was conducted using the `gamultiobj` function in MATLAB. Finally, the optimal time constants were programmed onto the FPGA. During a one-minute measurement period, the pile-up signals were reconstructed and discriminated in real time, after which the recovery of the spectra was analyzed.

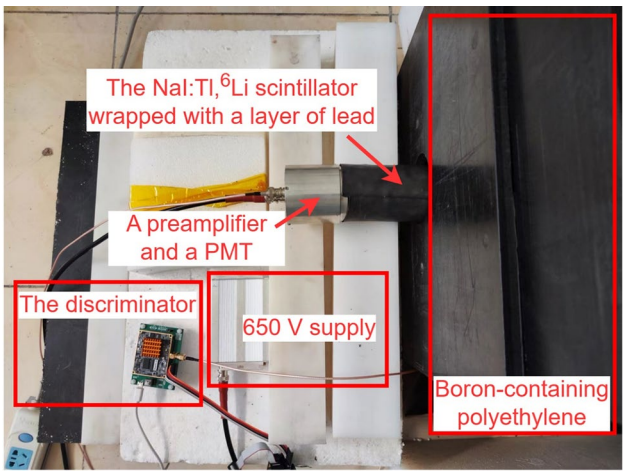

Fig. 4 (Color online) Experimental setup outside the ^{241}Am-Be source

4 Results and discussion

4.1 Validation of the pulse shaping algorithm

Pile-up events occur occasionally during nuclear radiation detection. At low count rates, these events are rare and may be regarded as part of statistical fluctuations. However, at high count rates, high-frequency pile-up events become significant and cannot be ignored. The closer the two pulse signals are spaced, the greater the impact; for example, the amplitude of the second pulse in a pile-up event may be falsely identified as being higher. Moreover, when two overlapping signals are extremely close, pile-up correction becomes even more challenging.

Figure 5a–c depict neutron and gamma signals with different amplitudes, along with artificially constructed pile-up

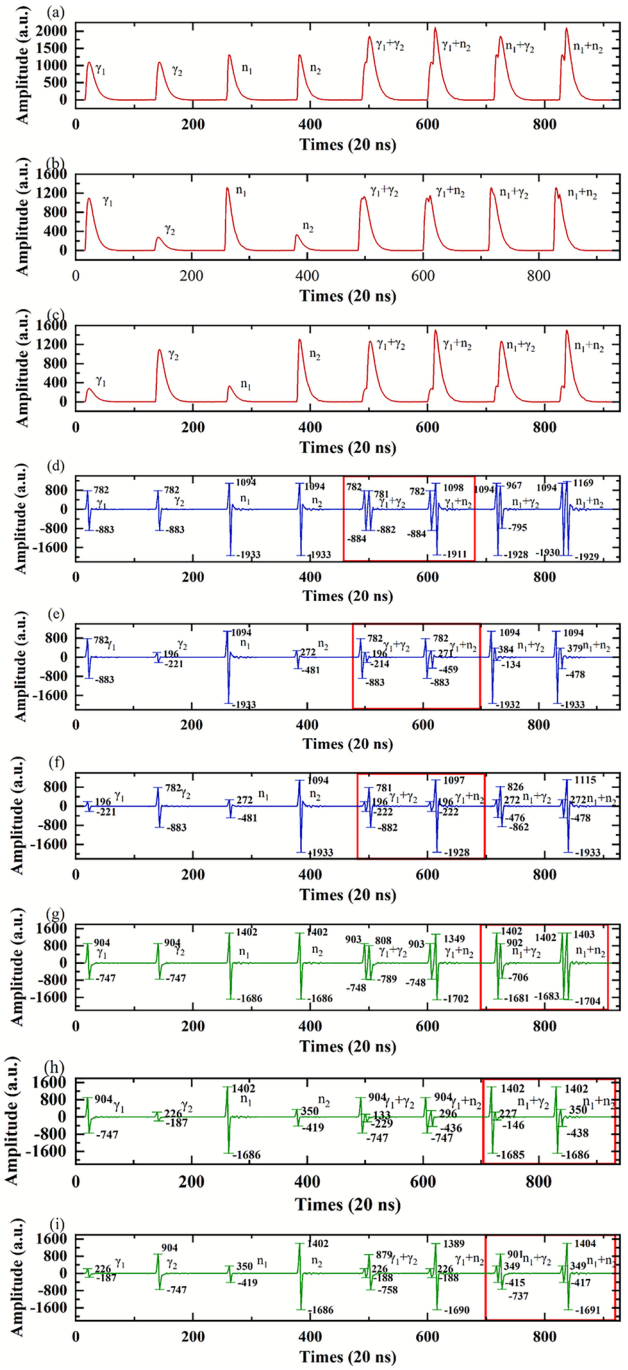

Fig. 5 (Color online) Manually constructed pile-up events include: **a** similar amplitude pulses, **b** small-amplitude pulses added to large-amplitude pulses, and **c** large-amplitude pulses added to small-amplitude pulses. The decay time constants for PSAG are 103.79 ns and 195.886 ns. **d–f** Bipolar cusp-like shaping results of **a–c** using PSAG. The decay time constants for PSAN are 43.864 ns and 209.4 ns. **g–i** Bipolar cusp-like shaping results of **a–c** using PSAN

events generated by adding one signal to another with a delay of eight clocks (160 ns). Such pile-up events severely distort the pulse waveform, causing two overlapping pulses to appear as a single pulse. The second pulse, which overlaps with the first, is erroneously detected by the peak detection algorithm with an exaggerated amplitude. Consequently, the standard peak detection algorithm not only detects the pile-up event as a pulse but also incorrectly extracts it with a large amplitude.

Figure 5d–f and g–i shows the bipolar cusp-like shaping results using PSAG (blue curve) and PSAN (green curve), respectively. The thick red line highlights the successfully separated pile-up signals, indicating that signals with different amplitudes can be restored to their original shapes without compromising particle discrimination and amplitude recovery. Accurate amplitude recovery is possible only if the first shaped signal in a pile-up event quickly returns to the baseline. Regardless of the signal amplitude, the shaped neutron signals consistently exhibit a significant trough amplitude. The separated signals maintain the same characteristics as the individually shaped signals, making particle discrimination more reliable than amplitude recovery. PSAG and PSAN each utilize their own criteria for classifying neutron and gamma signals due to the differences in their shaping results. Figure 5d and g shows that PSAG has a greater advantage in distinguishing the two types. In particular, the large trough in the neutron signal produced by PSAG yields a peak-to-valley ratio of 1094/1933 in Fig. 5d, which is smaller than that in Fig. 5g (1402/1686).

Figure 5d–i shows that the amplitudes of the shaped pile-up signals exhibit slight deviations compared to those of the individually shaped signals. In the case of n+γ pile-up events shown in Fig. 5i, for instance, the amplitude of the gamma signal (901) is reduced by 3 channels compared to its amplitude in isolation (904), resulting in a three-channel shift in the spectrum. The primary cause of these deviations is fixed-point arithmetic errors. As illustrated in Fig. 1, each operator in the algorithm produces a maximum of 16 fractional bits, while the final output is a 16-bit integer; fractional bits are dropped to produce integer channels. In addition, the use of a bi-exponential model for algorithm derivation introduces discrepancies, as the actual nuclear signal does not perfectly adhere to this model. Even after adjusting the decay time constant parameters, the shaped signal fluctuates around the baseline, so that the subsequent signal in a pile-up event is superimposed on this fluctuation rather than on a flat baseline. These slight deviations are considered tolerable and can be treated as statistical fluctuations in the energy spectrum measurements when accurate neutron counting is ensured.

4.2 Multi-objective optimization of the decay time constants

Before implementing the pulse shaping algorithm on the FPGA, the decay time constant parameters were obtained using MATLAB. Two decay time constants, ranging from

0 to 400 ns, were used as decision variables. The multi-objective optimization results for PSAG, using these two decay time constants, are shown in Fig. 6. As Fig. 5 suggests, optimization for PSAG primarily considers the γ+n and γ+γ pile-up cases. The discrimination ability σ, calculated using Eq. 24, is directly proportional to τ_1 and τ_2 within a certain range (Fig. 6a). In particular, σ approaches 0.3 as τ_1 increases to 240 ns and τ_2 to 120 ns. Although a larger σ generally indicates better discrimination, excessively large decay time constants may distort the bipolar cusp-like target shape and hinder amplitude recovery.

Figure 6b and c illustrates the second signal's amplitude recovery ability in γ+n and γ+γ pile-up cases. A smaller λ value indicates better amplitude recovery, and only specific combinations of τ_1 and τ_2 yield λ values close to zero. In these cases, τ_1 and τ_2 best fit the bi-exponential model of the gamma signal, likely resulting in the target bipolar cusp-like shapes shown in Fig. 5d–f. Moreover, amplitude recovery primarily depends on τ_2, which characterizes the fast component of the signal. τ_2 must be approximately 100 ns to ensure good amplitude recovery (small λ) while maintaining a sufficiently high σ (above 0.2). By considering λ_1 and λ_2 as optimization objectives, decay time constants that best fit the bi-exponential model of the gamma signal can be identified, giving amplitude recovery a greater weight than discrimination ability.

Figure 6d presents the Pareto front obtained with a population size of 500 using MATLAB's `gamultiobj` function, which finds the optimal decay time constants with high precision within the range of 0 to 400 ns. Although the Pareto frontier provides a series of optimal high-precision solutions, the hardware implementation of the pulse shaping algorithm runs in fixed-point arithmetic. Therefore, arbitrarily choosing one of these high-precision solutions does not affect the final shaping results because of the rounding that occurs after each operation (as shown in Fig. 1).

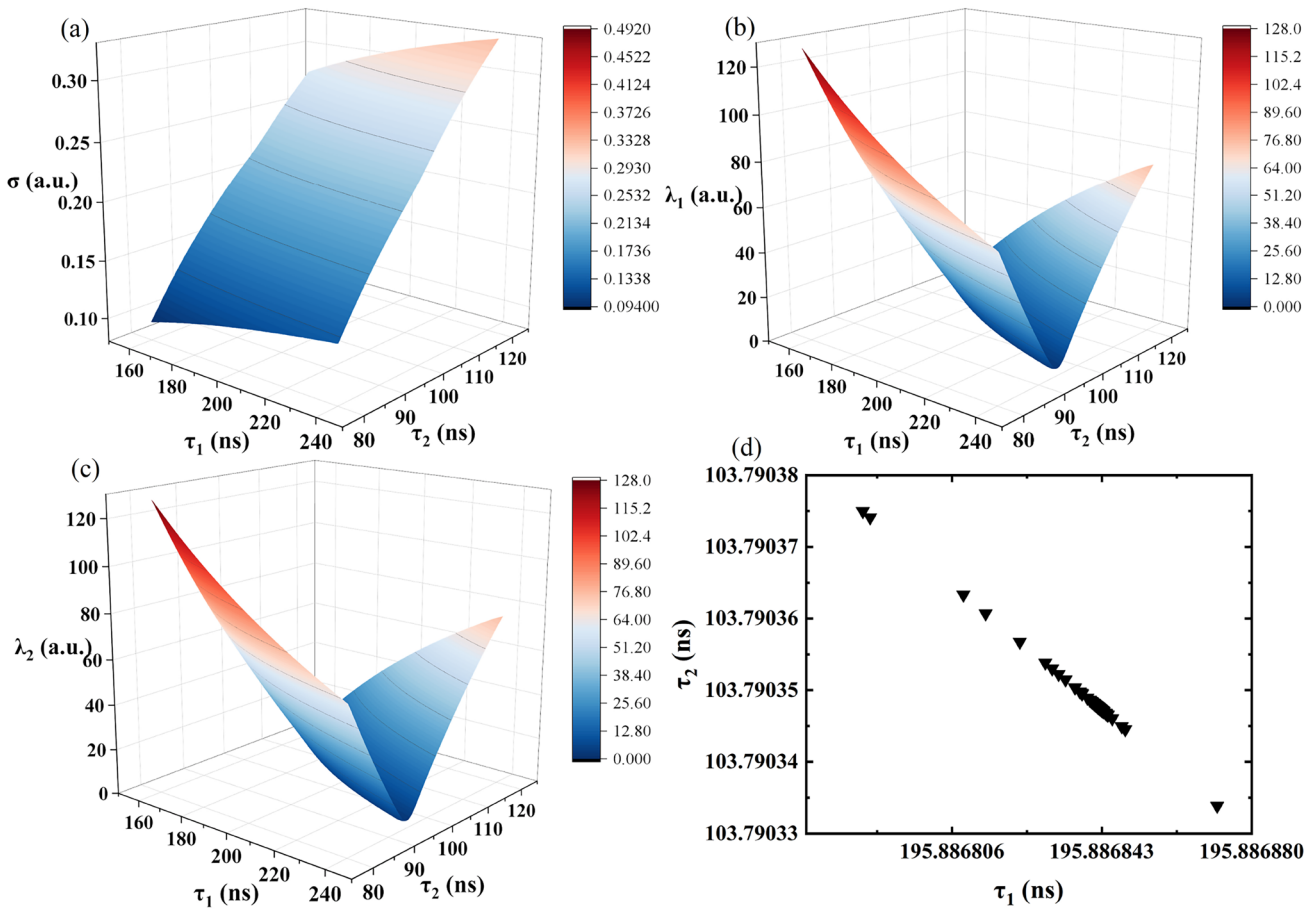

Fig. 6 (Color online) **a** Variation of the discrimination ability σ in γ+n pile-up event as a function of two decay time constants. Amplitude recovery **b** in the γ+γ pile-up event (λ_1) and **c** in the γ+n pile-up event (λ_2) vary with two decay time constants. **d** Pareto-optimal front of two decay time constants

4.3 Spectra restoration

During the high-count-rate online experiment, pile-up events involving multiple pulses were specifically extracted using an Integrated Logic Analyzer (ILA), as shown in Fig. 7. The NaIL detector in this study produced output signals with widths ranging from 200 to 500 ns. Neutron signals typically have widths of less than 300 ns, while gamma signals are usually wider (exceeding 300 ns). Given the higher prevalence of gamma signals, pile-up events are more likely to consist primarily of gamma pulses. The real-time shaping results observed on the FPGA were consistent with those in Fig. 5; both algorithms effectively shortened the pulse width and separated the accumulated signals. After pulse shaping, as shown in Fig. 7b and c, a signal with a notably smaller peak-to-valley ratio was observed and classified as a neutron signal by the algorithm.

The online implementation of the algorithm exhibits the same inaccuracies in magnitude recovery as shown in Fig. 5, leading to slight deviations in channel addresses. These inaccuracies result from several factors: (1) the shaping algorithm is an approximation derived from a bi-exponential signal; (2) the FPGA implementation relies on fixed-point computation, reducing accuracy; and (3) the input signal contains noise and other non-deterministic elements.

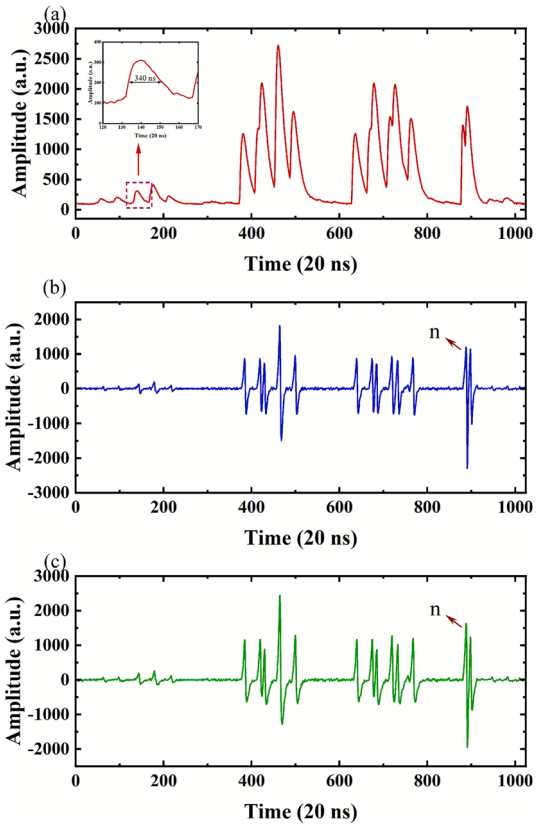

Fig. 7 (Color online) **a** Inverted pile-up signals from the NaIL detector output. Shaped signal outputs from **b** PSAG and **c** PSAN

In our previous study, the NaIL detector was positioned outside a boron-containing polyethylene shield with a 6-mm-thick lead layer, resulting in a lower count rate. At low count rates, the figures standard energy spectrum of the NaIL detector response to an ^{241}Am-Be source (shown by the green lines in Fig. 8c) was not processed by the filter shaping algorithm and was affected by only a small number of pile-up events, resulting in three distinct peaks that served as a benchmark for energy spectrum restoration.

As shown in Fig. 4, in the present study the NaIL detector was positioned inside a boron-containing polyethylene shield in close proximity to the source, leading to a high count rate and a substantial number of low-energy gamma rays from ^{241}Am. In practice, this abundance of low-energy gamma rays causes baseline fluctuations. Although a lead shield was wrapped around the NaIL scintillator to block gamma rays (as shown in Fig. 4), low-amplitude gamma signals were still observed (see Fig. 7), causing baseline instability.

The purple line in Fig. 8c shows the distorted energy spectrum at a high count rate. Owing to extensive pile-up events, the spectral peaks become less pronounced and the counts shift toward the high-energy region. Although the total counts in the two spectra of Fig. 8c are similar, the number of false counts increases significantly in the energy region above 5000 keV. Because low-energy gamma counts are very high and neutrons are nearly absent in the low-energy region, an energy threshold of 244 keV was set so that signals below this threshold were excluded.

Figure 8a and b illustrates the PSD performance of PSAG and PSAN, respectively. The figure of merit (FoM), first introduced by Winyard et al. [46], is given by:

$$\mathrm{FoM} = \frac{S}{\mathrm{FWHM}_{\gamma} + \mathrm{FWHM}_{\mathrm{n}}}, \tag{25}$$

where S represents the distance between the centroids of the gamma and neutron peaks, and FWHM_{γ} and $\mathrm{FWHM}_{\mathrm{n}}$ are the full widths at half maximum of the gamma and neutron peaks, respectively.

Figure 8a and b shows that while both PSAG and PSAN yield similar distributions, the neutron and gamma peaks are more widely separated in the PSD plot obtained by PSAG, indicating superior PSD capability. As previously mentioned, the pulse shaped by PSAG has a greater peak-to-valley ratio, resulting in a higher FoM. After determining $\lambda_{\mathrm{standard}}$ from the PSD plots, signal types can be classified based on $\lambda_{\mathrm{standard}}$ to obtain the separated energy spectra shown in Fig. 8d. For example, PSAG output signals with λ less than 0.492 (represented as 0x07DF on the FPGA) are classified as neutron signals.

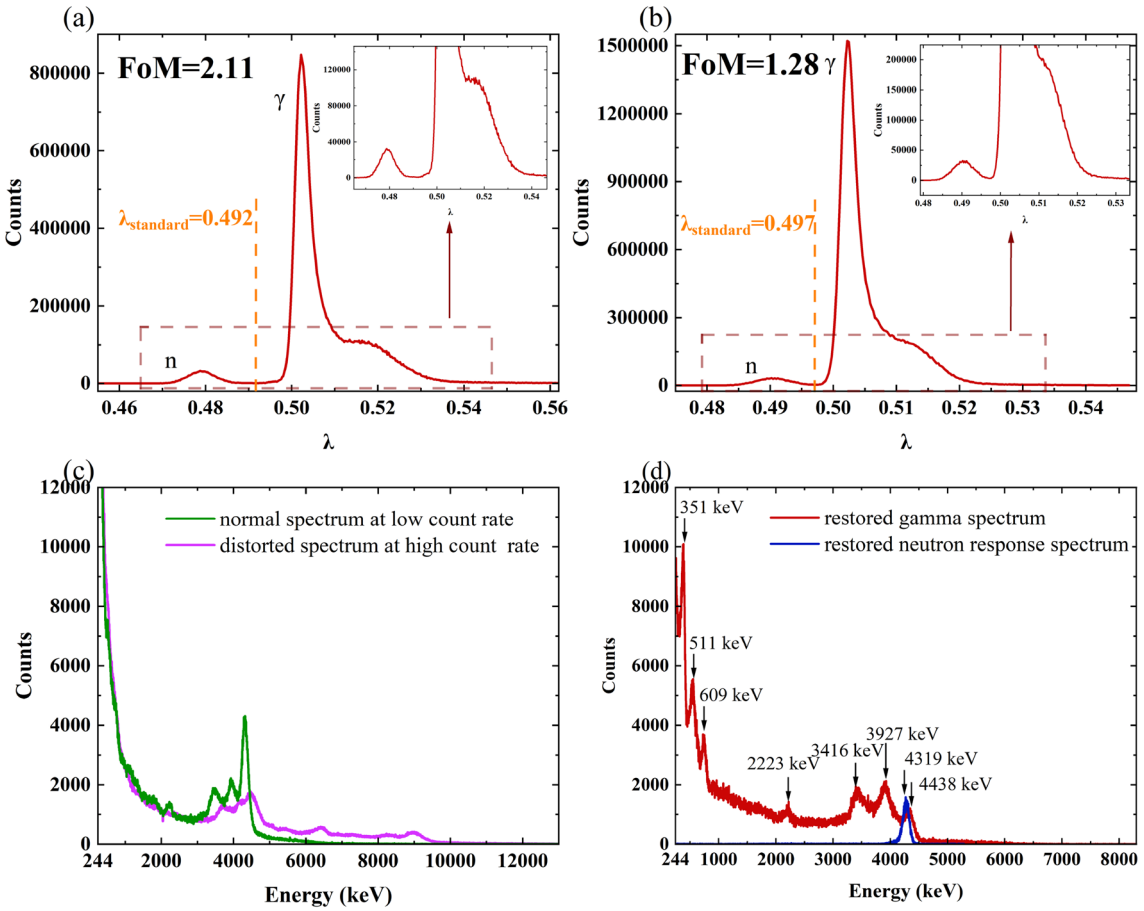

Fig. 8 (Color online) PSD and energy spectrum analyses. **a** PSD plot obtained using PSAG and measured over one minute. **b** PSD plot obtained using PSAN and measured over one minute. **c** Energy spectrum distortion due to increased count rate: the green spectrum was measured over five minutes at 10584 cps, whereas the purple spectrum was measured over one minute at 59257 cps. **d** Restoration and separation of the spectrum applying both PSAG and PSAN in a one-minute measurement: the gamma spectrum was measured at 58374 cps and the neutron response spectrum at 2804 cps. Only counts above 244 keV were recorded in these spectra

It is noteworthy that Fig. 8b shows more total counts than Fig. 8a, even though both PSAG and PSAN process the same input signals in parallel. This is because the same channel address threshold was imposed in the hardware, and PSAN tends to increase the overall amplitude of the signals, resulting in more signals exceeding the threshold. However, due to the presence of a coincidence system, excess counts from PSAN were not included in the final energy spectrum.

As shown in Fig. 8d, the coincidence system combining PSAG and PSAN is capable of restoring the normal neutron and gamma energy spectra from the pile-up-affected spectrum shown in Fig. 8c. However, the restored spectra in Fig. 8d exhibit noticeable noise and lack smoothness, resulting in fluctuations and irregularities in the spectral peaks. This noise may stem from statistical fluctuations in detection, electronic noise in the measurement system, or inaccuracies introduced by the FPGA implementation of the shaping algorithm.

Despite these inaccuracies, the application of the shaping algorithm resulted in more pronounced spectral peaks. The ^{241}Am-Be source used in this study primarily emitted a large number of low-energy gamma rays. Although this alone did not cause severe distortion at a count rate of 10 kcps, a noticeable number of pile-up events still occurred in the low-energy region. Consequently, the spectral peaks in the low-energy region (as shown in Fig. 8c) are not distinct when no filtering is applied, but become more pronounced after applying the proposed narrow shaping algorithm, demonstrating the algorithm's capability to improve the signal-to-noise ratio.

The highest energy gamma-ray peak corresponds to the full-energy peak at 4438 keV from the de-excitation of ^{12}*C produced in the reaction $\alpha(^{9}\mathrm{Be}, \mathrm{n})^{12}$*C [47]. Adjacent to this full-energy peak, a single escape peak occurs at 3927 keV and a double escape peak at 3416 keV. In addition, hydrogen nuclei in the polyethylene shield captured thermal neutrons, producing gamma rays at 2230 keV. In the low-energy

region, ^{214}Pb and its beta-decay product ^{214}Bi emit gamma rays at 351 keV and 609 keV, respectively, and a 511 keV peak due to positron annihilation is also observed. These low-energy peaks become visible after pulse shaping.

In a NaIL scintillator, neutrons are indirectly detected through their reaction with ^{6}Li [44]:

$$^{6}_{3}\mathrm{Li} + ^{1}_{0}\mathrm{n} \rightarrow ^{3}_{1}\mathrm{H} + \frac{4}{2}\alpha + 4.78\,\mathrm{MeV}, \sigma = 940\,\mathrm{b}. \quad (26)$$

This reaction produces tritium and alpha particles with a total energy release of 4.78 MeV. The high neutron response energy captured by ^{6}Li precludes particle discrimination in the low-energy region. Due to the finite fluorescence efficiency of the charged particles in NaIL scintillators, a single neutron response peak appears at 4319 keV in the gamma energy spectrum. The position of the neutron response peak in the gamma spectrum depends on the experimental setup. Lai et al. reported that the luminous efficiency of alpha and tritium particles in NaIL crystals was approximately 70%, resulting in a neutron response peak close to the double escape peak [48]. Figure 5 demonstrates that a pulse shaping algorithm produces different gains for neutron and gamma signals. In [40], signals processed using a trapezoidal shaper with different gains for neutrons and gammas resulted in a neutron response peak close to a single escape peak. In Fig. 8c, the amplitudes at the NaIL detector output are recorded without filtering or shaping. As shown in Fig. 8d, the thermal neutron response energy is centered at 4319 keV, which is close to the energy released by ^{12*}C. The separated neutron response spectrum also indicates that the NaIL detector, when placed adjacent to the ^{241}Am-Be source, recorded 2804 neutron events per second.

5 Conclusion

A bipolar pulse shaping algorithm was introduced to address pile-up events involving different particle types. At count rates of approximately 60000 cps for signals above 244 keV, this algorithm was successfully implemented on an FPGA in real time, achieving reliable particle discrimination and amplitude recovery for pile-up events. This method does not rely on large datasets and only requires the extraction of the decay time constants for individual neutron and gamma signals—a process that can be accomplished through multi-objective optimization using MATLAB. By adjusting only a few parameters, the IP core of this algorithm can be easily deployed on other FPGA-based instruments. However, to guarantee accurate amplitude recovery in pile-up events, two parallel shaping algorithms are required, which increases the complexity of logic control. Future research on innovative pulse shapes may help simplify the algorithmic structure. In addition, due to the high neutron response energy at the output of the NaIL detector, neither the PSD plots nor the acquired spectra contain counts at energies below 244 keV. Further spectroscopic analysis is required to compare the performance of this method with that of other scintillators.

Author Contributions All authors contributed to the study conception and design. Material preparation, data collection, and analysis were performed by J-XL and H-LH The first draft of the manuscript was written by JL, and all authors commented on previous versions of the manuscript. All authors read and approved the final manuscript.

Data availability The data that support the findings of this study are openly available in Science Data Bank at https://cstr.cn/31253.11.sciencedb.j00186.00784 and https://doi.org/10.57760/sciencedb.j00186.00784.

Declarations

Conflict of interest The authors declare that they have no conflict of interest.

References

1. X.K. Ma, H.Q. Huang, B.R. Huang et al., X-ray spectra correction based on deep learning CNN-LSTM model. Measurement **199**, 111510 (2022). https://doi.org/10.1016/j.measurement.2022.111510
2. J. Liu, J. Yang, G.Q. Zeng et al., Implementation of a cusp-like for real-time digital pulse shaper in nuclear spectrometry. Nucl. Sci. Tech. **28**, 103 (2017). https://doi.org/10.1007/s41365-017-0248-1
3. Y.Q. Zhang, L.Q. Hu, G.Q. Zhong et al., Development of a high-speed digital pulse signal acquisition and processing system based on MTCA for liquid scintillator neutron detector on EAST. Nucl. Sci. Tech. **34**, 10 (2023). https://doi.org/10.1007/s41365-023-01318-9
4. Y. Liu, M. Wang, W.J. Wang et al., Counting-loss correction method based on dual-exponential impulse shaping. J. Synchrotron Radiat. **27**, 1609–1613 (2020). https://doi.org/10.1107/S1600577520010954
5. A. Sahlberg, J. Eriksson, S. Conroy et al., Forward modeling of pile-up events in liquid scintillator detectors for neutron emission spectroscopy. Rev. Sci. Instrum. **92**, 083502 (2021). https://doi.org/10.1063/5.0052260
6. J. Yu, J.B. Zhou, X.G. Tuo et al., Sum peak probability estimation in radiation measurement. Measurement **174**, 109023 (2021). https://doi.org/10.1016/j.measurement.2021.109023
7. X.F. Xu, S.P. Li, H.R. Cao et al., The neutron-gamma pulse shape discrimination method for neutron flux detection in the ITER. Plasma Sci. Technol **15**, 5 (2013). https://doi.org/10.1088/1009-0630/15/5/04
8. X.D. Zhong, L. Chen, B.C. Wang et al., A spectrometer with baseline correction and fast pulse pile-up rejection for prompt gamma neutron activation analysis technology. Rev. Sci. Instrum. **89**, 123504 (2018). https://doi.org/10.1063/1.5049517
9. X.L. Luo, V. Modamio, J. Nyberg et al., Pulse pile-up identification and reconstruction for liquid scintillator based neutron detectors. Nucl. Instrum. Methods Phys. Res. A **897**, 59–65 (2018). https://doi.org/10.1016/j.nima.2018.03.078
10. Q. Wang, C. Wang, Z. Wang et al., Achieving efficient neutron and gamma discrimination in a highly stable ^{6}Li-loaded $Cs_3Cu_2I_5$

perovskite scintillator. J. Phys. Chem. Lett. **13**, 9066–9071 (2022). https://doi.org/10.1021/acs.jpclett.2c02643
11. J. Glodo, R. Hawram, E. Loef et al., Pulse shape discrimination with selected elpasolite crystals. IEEE Trans. Nucl. Sci. **59**, 5 (2012). https://doi.org/10.1109/TNS.2012.2188646
12. J. Han, J. Zhu, Z. Wang et al., Pulse characteristics of CLYC and piled-up neutron-gamma discrimination using a convolutional neural network. Nucl. Instrum. Methods Phys. Res. A **17**, 166328 (2022). https://doi.org/10.1016/j.nima.2022.166328
13. S.X. Liu, W. Zhang, Z.H. Zhang et al., Performance of real-time neutron/gamma discrimination methods. Nucl. Sci. Tech. **34**, 8 (2023). https://doi.org/10.1007/s41365-022-01160-5
14. I.R. Morales, M.L. Crespo, M. Bogovac et al., Gamma/neutron classification with SiPM CLYC detectors using frequency-domain analysis for embedded real-time applications. Nucl. Eng. Technol. **56**, 745–752 (2024). https://doi.org/10.1016/j.net.2023.11.013
15. F.Z. Shen, Q.B. Fu, T.C. Huang et al., A compact dual gamma neutron detector based on NaI(Tl+Li) scintillator readout with SiPM. Crystals **12**, 8 (2022). https://doi.org/10.3390/cryst12081077
16. M. Polo, F. Pino, J.C.A. Delgado et al., Assessment of a NaIL detector performance for radiation monitoring applications. Eur. Phys. J. Spec. Top. **232**, 1477–1486 (2023). https://doi.org/10.1140/epjs/s11734-023-00896-4
17. X.F. Wen, A. Enqvist, Pulse shape discrimination of $Cs_2LiYCl_6:Ce^{3+}$ detectors at high count rate based on triangular and trapezoidal filters. Nucl. Instrum. Methods Phys. Res. A **866**, 129–133 (2017). https://doi.org/10.1016/j.nima.2017.06.007
18. C. Fu, A. Di Fulvio, S.D. Clarke et al., Artificial neural network algorithms for pulse shape discrimination and recovery of piled-up pulses in organic scintillators. Ann. Nucl. Energy **120**, 410–421 (2018). https://doi.org/10.1016/j.anucene.2018.05.054
19. S. Peng, Z.H. Hua, Q. Wu et al., Piled-up neutron-gamma discrimination system for CLLB using convolutional neural network. J. Instrum. **17**, T08001 (2022). https://doi.org/10.1088/1748-0221/17/08/T08001
20. H.R. Liu, Y.X. Cheng, Z. Zuo et al., Discrimination of neutrons and gamma rays in plastic scintillator based on pulse-coupled neural network. Nucl. Sci. Tech. **32**, 82 (2021). https://doi.org/10.1007/s41365-021-00915-w
21. X. Fabian, G. Baulieu, L. Ducroux et al., Artificial neural networks for neutron/ γ discrimination in the neutron detectors of NEDA. Nucl. Instrum. Methods Phys. Res. A **986**, 164750 (2021). https://doi.org/10.1016/j.nima.2020.164750
22. N. Mauritzson, K.G. Fissum, J.R.M. Annand et al., Technique for the measurement of intrinsic pulse-shape discrimination for organic scintillators using tagged neutrons. Nucl. Instrum. Methods Phys. Res. A **1039**, 167141 (2022). https://doi.org/10.1016/j.nima.2022.167141
23. A. Hachem, Y. Moline, G. Corre et al., Labeling strategy to improve neutron/gamma discrimination with organic scintillator. Nucl. Eng. Technol. **55**, 4057–4065 (2023). https://doi.org/10.1016/j.net.2023.07.024
24. M. Amiri, V. Přenosil, F. Cvachovec et al., Quick algorithms for real-time discrimination of neutrons and gamma ray. J. Radioanal. Nucl. Chem. **303**, 583–599 (2015). https://doi.org/10.1007/s10967-014-3406-5
25. G.F. Knoll, *Radiation Detection and Measurement* (Wiliey, New York, 2010). https://doi.org/10.1118/1.4729840
26. J.B. Zhou, Y. Liu, X. Hong et al., Trapezoidal pulse shaping for pile-up pulse identification in X-ray spectrometry. Chin. Phys. C **39**, 6 (2015). https://doi.org/10.1088/1674-1137/39/6/068201
27. J.Y. Li, P. Fan, C.L. Zhu et al., Optimization of pulse shape discrimination based on frequency domain for SiPM-based NaIL scintillator detector. J. Inst. **19**, 3 (2024). https://doi.org/10.1088/1748-0221/19/03/P03014
28. H. Arahmane, A. Mahmoudi, E.-M. Hamzaoui et al., Neutron-gamma discrimination based on support vector machine combined to nonnegative matrix factorization and continuous wavelet transform. Measurement **149**, 106958 (2020). https://doi.org/10.1016/j.measurement.2019.106958
29. H. Arahmane, E.-M. Hamzaoui, Y. Ben Maissa et al., Neutron-gamma discrimination method based on blind source separation and machine learning. Nucl. Sci. Tech. **32**, 18 (2021). https://doi.org/10.1007/s41365-021-00850-w
30. X.F. Yang, H.Q. Huang, G.Q. Zeng et al., Pulse pile-up correction by particle swarm optimization with double-layer parameter identification model in X-ray spectroscopy. J. Sign. Process. Syst. **94**, 377–386 (2022). https://doi.org/10.1007/s11265-021-01698-4
31. M.S. El_Tokhy, Advanced algorithms for retrieving pileup peaks of digital alpha spectroscopy using antlions and particle swarm optimizations. Nucl. Sci. Tech. **31**, 37 (2020). https://doi.org/10.1007/s41365-020-0745-5
32. V.T. Jordanov, Unfolding-synthesis technique for digital pulse processing, part 1: unfolding. Nucl. Instrum. Methods Phys. Res. A **805**, 63–71 (2016). https://doi.org/10.1016/j.nima.2015.07.040
33. V.T. Jordanov, K.V. Jordanova, Unfolding-synthesis technique for digital pulse processing, Part 2: synthesis. Nucl. Instrum. Methods Phys. Res. A **1004**, 167421 (2022). https://doi.org/10.1016/j.nima.2022.167421
34. Z.J. Qin, C. Chen, J.S. Luo et al., A pulse-shape discrimination method for improving Gamma-ray spectrometry based on a new digital shaping filter. Radiat. Phys. Chem. **145**, 193–201 (2018). https://doi.org/10.1016/j.radphyschem.2017.10.023
35. R.X. Liu, H.R. Liu, Y. Bo et al., Heterogeneous quasi-continuous spiking cortical model for pulse shape discrimination. Electronics **12**, 2234 (2023). https://doi.org/10.3390/electronics12102234
36. M. Nakhostin, A technique for the reduction of pulse pile-up effect in pulse-shape discrimination of organic scintillation detectors. Nucl. Eng. Technol. **52**, 360–365 (2020). https://doi.org/10.1016/j.net.2019.07.035
37. V.T. Jordanov, *Pile-up real time pulse-shape discrimination based on ballistic deficit measurement and digital time-invariant pulse shaping*, in *IEEE Nuclear Science Symposium and Medical Imaging Conference Proceedings (NSS/MIC)* (2018), pp. 1–5. https://doi.org/10.1109/NSSMIC.2018.8824502
38. V. Esmaeili-sani, A. Moussavi-zarandi, N. Akbar-ashrafi et al., Neutron-gamma discrimination based on bipolar trapezoidal pulse shaping using FPGAs in NE213. Nucl. Instrum. Methods Phys. Res. A **694**, 164372 (2012). https://doi.org/10.1016/j.nima.2012.08.025
39. M. Kafaee, A. Moussavi-Zarandi, Baseline restoration and pile-up correction based on bipolar cusp-like shaping for high-resolution radiation spectroscopy. J. Korean Phys. Soc. **68**, 8 (2016). https://doi.org/10.3938/jkps.68.960
40. J.X. Li, H.L. Hou, Y.F. Huang et al., Pulse-shaping method for real-time neutron/gamma discrimination at low sampling rates. Nucl. Sci. Tech. **34**, 165 (2023). https://doi.org/10.1007/s41365-023-01306-z
41. Q.T. Wang, H.Q. Huang, X.K. Ma et al., Trapezoidal pile-up nuclear pulse parameter identification method based on deep learning transformer model. Appl. Radiat. Isot. **190**, 110515 (2022). https://doi.org/10.1016/j.apradiso.2022.110515
42. Z.Q. Cheng, Q.X. Zhang, H.Y. Tan et al., Self-adaptive pulse shape identification by using Gaussian mixture model. Radiat. Meas. **172**, 107067 (2024). https://doi.org/10.1016/j.radmeas.2024.107067
43. K. Deb, *Multi-objective Optimization Using Evolutionary Algorithms* (Wiley, New York, 2001). https://doi.org/10.1007/978-0-85729-6528_1
44. K. Yang, P.R. Menge, V. Ouspenski, Li co-doped NaI: Tl (NaIL)—a large volume neutron-gamma scintillator with exceptional pulse

shape discrimination. IEEE Trans. Nucl. Sci. **64**, 8 (2017). https://doi.org/10.1109/TNS.2017.2721398
45. J.L. Zhang, E.M. Michael, Z.H. Wang et al., Study of sampling rate influence on neutron-gamma discrimination with stilbene coupled to a silicon photomultiplier. Appl. Radiat. Isot. **128**, 120–124 (2017). https://doi.org/10.1016/j.apradiso.2017.06.036
46. R.A. Winyard, J.E. Lutkin et al., Pulse shape discrimination in inorganic and organic scintillators. I. Nucl. Instrum. Methods **95**, 141–153 (1971). https://doi.org/10.1016/0029-554X(71)90054-1
47. S. Croft, The use of neutron intensity calibrated ^{9}Be(α, n) sources as 4438 keV gamma-ray references standards. Nucl. Instrum. Methods Phys. Res. A **281**, 103–116 (1989). https://doi.org/10.1016/0168-9002(89)91221-7
48. C.F. Lai, J.G. Qin, J. Xiao et al., Particle discrimination and fast neutron response for a NaIL: Tl and a NaI: Tl scintillator detector. Nucl. Instrum. Methods Phys. Res. A **978**, 164372 (2020). https://doi.org/10.1016/j.nima.2020.164372